Available online at www.sciencedirect.com
SCIENCE DIRECT®
Applied Geochemistry 21 (2006) 223–240
Applied Geochemistry
www.elsevier.com/locate/apgeochem

Computer simulation of CO_2 trapped through mineral precipitation in the Rose Run Sandstone, Ohio

Biniam Zerai *, Beverly Z. Saylor, Gerald Matisoff

Department of Geological Sciences, Case Western Reserve University, 10900 Euclid Avenue, Cleveland, OH 44106, USA

Received 19 August 2004; accepted 2 November 2005
Editorial handling by R. Fuge

Abstract

Equilibrium, path-of-reaction and kinetic modeling of CO_2–brine–mineral reactions in the Rose Run Sandstone, one of Ohio's deep saline aquifers, was conducted in order to investigate the factors that are likely to influence the capacity of this formation to trap injected CO_2 as solid carbonate mineral phases. Equilibrium modeling was applied to investigate the impact of temperature, pressure, mineralogy, brine composition, and CO_2 fugacity on mineral dissolution and precipitation, the amount of CO_2 sequestered, and the form of sequestration. Path of reaction and kinetic modeling were used to evaluate intermediate products and reaction progress as a function of time, as well as to investigate the impact of brine-to-rock ratio. The results of equilibrium modeling demonstrate that dissolution of albite, K-feldspar, and glauconite, and the precipitation of dawsonite and siderite are potentially very important for mineral trapping of CO_2. According to the path of reaction and kinetic modelling, the stability of carbonate rocks is controlled by the brine-to-rock ratio, the pH of the system, the fugacity of CO_2, and the kinetic rate of dissolution. In kinetic modeling, with a brine-to-rock ratio of 1:25, reactive surface area of 10 cm^2/g, 10 MPa f_{CO_2}, and 12% porosity (1.5–2 g of CO_2 per kg of reacted rock), significant quantities (10–40 g) of carbonate minerals were precipitated from both the sandstone and mixed rock assemblages. The Rose Run Sandstone has the potential to store CO_2 over millennia as a negatively buoyant aqueous solution and, ultimately, as immobile carbonate minerals.

1. Introduction

Growing concern about human-induced climate change is driving technology development aimed at slowing the buildup of greenhouse gases in the atmosphere. One approach is to increase the storage of waste CO_2 in reservoirs other than the atmosphere. Potential reservoirs include the terrestrial biosphere (Seneviratne, 2003), the oceans (Drange et al., 2001), mineralized forms at the Earth's surface (Lackner, 2002), and deep subsurface sedimentary formations (Holloway, 2001). Injection of CO_2 deep underground is particularly promising because deep sedimentary formations have the potential to store large volumes of CO_2, safely, and to retain the CO_2 in the subsurface for thousands to millions of years. Deep sedimentary formations include deep, unmineable coal seems, depleted oil and gas reservoirs, and deep saline aquifers (Bachu, 2002).

* Corresponding author. Fax: +1 216 368 3691.
E-mail address: bxz11@case.edu (B. Zerai).

0883-2927/$ - see front matter © 2006 Elsevier Ltd. All rights reserved.
doi:10.1016/j.apgeochem.2005.11.002

Deep saline aquifers provide the largest potential subsurface storage capacity for injected CO_2. In the United States, deep saline aquifers have a larger potential storage capacity than any other type of sedimentary formation, with estimates as high as 500 Gt of CO_2 storage (Bergman and Winter, 1995). In addition to the large potential capacity, deep aquifers hold promise because they are widespread and are found in close proximity to point sources of emissions, such as electric power plants (Bachu et al., 1994).

Once injected, free CO_2, which is less dense than formation fluids, will rise buoyantly until it reaches an impermeable or low permeability seal. Theoretically, the CO_2 can be prevented from further migration toward the surface by slow moving, downward-directed formation waters. Escape through a leaky seal, especially a seal that is punctured by high permeability vertical flow paths such as faults and fractures is a risk (Klusman, 2003). However, some CO_2 dissolves into the pore water and the CO_2–brine solution is negatively buoyant, increasing storage safety. Safe, permanent storage requires that over time, the injected CO_2 dissolve in the formation waters and through reactions with the formation's minerals be converted to carbonate mineral phases, resulting in mineral trapping of CO_2 as an immobile, solid form (Gunter et al., 1997).

This paper presents results of equilibrium, path-of-reaction, and kinetic modeling of CO_2–brine–mineral reactions in a sandstone and carbonate saline aquifer deep beneath eastern Ohio, USA. Equilibrium modeling of CO_2–brine–mineral reactions for typical mineral assemblages was applied to investigate the impact of temperature, pressure, mineralogy, brine composition, and CO_2 fugacity on mineral dissolution and precipitation, the amount of CO_2 sequestered, and the form of sequestration. Path of reaction modeling was utilized to evaluate intermediate products as progressively more mineral reacted with the CO_2 enriched brine. Kinetic modeling was used to investigate chemical reactions as a function of time in order to demonstrate the impact of reaction time scale on the resulting dissolution and precipitation products.

2. Geologic reservoir – Rose Run Sandstone

The Cambrian Rose Run Sandstone is a deep saline aquifer and oil-gas producing unit that extends beneath eastern Ohio, Pennsylvania, New York, and Kentucky in the Appalachian Basin of the eastern United States. It is a sandy layer in the middle of the Knox Dolomite. It is truncated by the Knox unconformity beneath central Ohio (Fig. 1) so that it thickens eastward from 0 m in central Ohio to 200 m in eastern Pennsylvania (Janssens, 1973; Riley et al., 1993). Erosional remnants and truncation along the angular unconformity form stratigraphic traps, and the subcrop belt, where the Rose Run Sandstone intersects the Knox unconformity, is the principal locale for oil and gas production from this unit in Ohio (Fig. 1).

The Rose Run Sandstone is considered a potential candidate for CO_2 sequestration because it is located close to many of Ohio's large coal-fired power plants (Fig. 1). Oil and gas fields within the formation may also provide localized CO_2 storage with a cost-incentive provided by enhanced oil recovery by CO_2 injection (Bachu, 2002). The Rose Run Sandstone also is the only one of the deep Cambrian sandstones beneath Ohio that is known to retain its sandstone composition in the eastern part of the state rather than passing laterally into carbonate (Gupta et al., 2004). The Rose Run Sandstone meets the general criteria for aquifer disposal of CO_2 outlined by Bergman and Winter (1995), Bergman et al. (1997) and Bachu (2002). Across much of eastern Ohio, it lies at depths greater than 800 m, the minimum depth necessary for injection of CO_2 as a dense, supercritical phase (Fig. 2). It is sealed by impermeable cap rock consisting of Ordovician age carbonate and shale, with a total thickness of 100–500 m beneath Ohio (Janssens, 1973; Riley et al., 1993). The regional flow is down-dip to the east and southeast (Gupta and Bair, 1997), as required for hydrodynamic trapping by downward-directed flow.

The Rose Run Sandstone consists of sandstone interbedded with dolostone (Fig. 3) and is heterogeneous at multiple scales (Janssens, 1973; Riley et al., 1993). Like many deep aquifers of the eastern United States and Canada, the sandstone of the Rose Run Sandstone is mature, consisting predominantly of quartz, with minor alkali feldspar and local glauconitic layers. The typical ranges of porosity and permeability of the sandstone layers of the Rose Run Sandstone are 7–15% and 1–15 md, respectively (Riley et al., 1993).

The brine of the Rose Run Sandstone is composed mainly of Na^+ and Cl^-, with subordinate Ca^{2+}, Mg^{2+}, Br^-, K^+, Sr^{2+}, SO_4^{2-}, Fe^{2+}, HCO_3^+, H^+, $SiO_2(aq)$, and Al^{3+} (Breen et al., 1985). The median concentration of total dissolved solids is

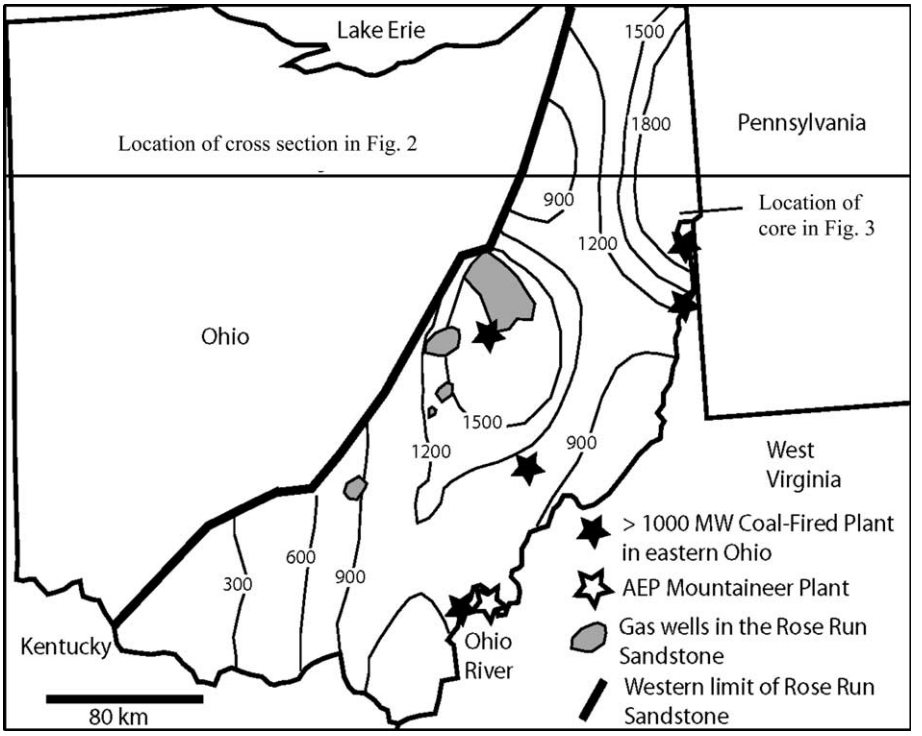

Fig. 1. Map showing depth to Knox unconformity where it overlies the Rose Run Sandstone in eastern Ohio. Contour interval in meters. AEP = American Electric Power.

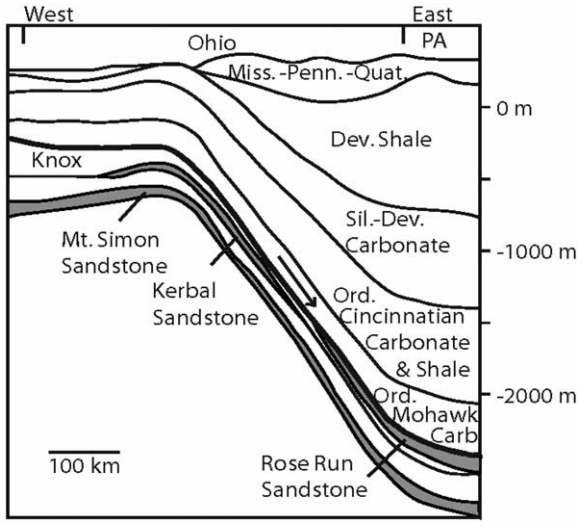

Fig. 2. Cross-section for central Ohio. Cambrian sandstones that are candidates for CO_2 storage are shaded (after Gupta and Bair, 1997). PA = Pennsylvania. For location of cross-section, see Fig. 1.

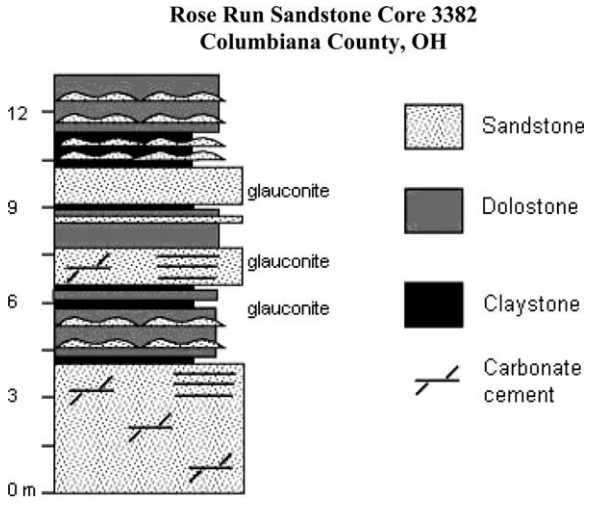

Fig. 3. Measured section of core through part of the Rose Run Sandstone. For location of core, see Fig. 1.

278,000 mg/kg (Breen et al., 1985). Recent work done by Gupta et al. (2004) indicates that the total dissolve solid concentration can reach more than 320,000 mg/kg.

3. Methods

3.1. Computer simulation

Geochemist's Workbench (GWB™) version 3.2.2 (Bethke, 1996) was used for equilibrium, path of

reaction, and kinetic modeling of CO_2–brine–mineral reactions. The Geochemist's Workbench is a chemical-reactor type, module-based software program that simulates chemical reactions under both equilibrium and kinetic conditions, calculates stability diagrams and equilibrium states of natural waters, and traces reaction processes. Equilibrium and path of reaction models are based on the thermodynamic data for the minerals involved in the reaction. Equilibrium modelling predicts the ultimate fate of the CO_2. Path of reaction modeling traces the progress of reactions by adding/removing small amounts of mineral reactant. Path of reaction modeling is important for investigating the precipitation and dissolution of phases as the reaction progresses. Kinetic modeling considers the rates of reactions based on appropriate rate constants. It permits computation of the time the system needs to start consuming and trapping CO_2 as precipitated mineral phases, as well as the time it takes the system to approach 'steady state' or dynamic equilibrium.

GWB requires that CO_2 pressure be input as fugacity. For a given fugacity and temperature, the effect of salinity on the solubility of CO_2 can be simulated by re-assigning the aqueous species CO_2(aq) an ionic size of −0.5 in the thermodynamic database. The effect of salting-out was modeled by adjusting the activity coefficient of CO_2 using a polynomial data fit developed by Helgeson (1969) which are functions of temperature and ionic strength of the solution. The activity coefficients of neutral species (like CO_2(aq)) are calculated from ionic strength using an empirical relationship (Helgeson, 1969; Bethke, 1996). These relationships are coded in the GWB to calculate the salting-out effect at higher ionic strengths (Bethke, 1996).

GWB does not take into account the flow of brine through the aquifer. Modeling the chemical reactions under no-flow conditions provides insight into the important variables that control reaction progress and reaction products such as the effect of fugacity, brine-to-rock ratio, type of mineral assemblage, and rate constants on CO_2 immobilization through carbonate precipitation can be assessed.

Geochemist's Workbench has an internal thermodynamic database and requires user input of kinetic rate data (Table 1). The following rate equation was adopted in the modeling (Lasaga, 1995):

$$\text{Rate} = \frac{\mathrm{d}n_i}{\mathrm{d}t} = KA_{\min} \exp\left(\frac{-E_a}{RT}\right)\left[\frac{Q}{K_{eq}} - 1\right] \qquad (1)$$

Table 1
Rate constants for silicate and carbonate minerals compiled from literature and used in the computer simulations

Mineral	Rate constants $\log K$ (mol/m^2 s)	References
Albite	−11	Sverdrup (1990)
Annite	−10.5	Acker and Bricker (1992)
Calcite	−5.8	Plummer et al. (1978)
Dolomite	−6.7	Busenberg and Plummer (1982)
Kaolinite	−11.4	Sverdrup (1990)
K-feldspar	−10.9	Helgeson et al. (1984)
Quartz	−12	Rimstidt and Barnes (1980)

where K is the rate constant (mol/cm^2 s), $A_{\min}$ is the reactive surface area (cm^2), E_a is the activation energy (J/mol), R is the gas constant (J/kmol), T is absolute temperature (K), Q is the activity product, and K_{eq} is the equilibrium constant. The rate constants used here are from the literature, based on laboratory experiments; laboratory measurements of rate constants can be several orders of magnitude greater than rates of weathering measured in the field (Lasaga, 1995). Spherical geometry of the minerals grains was assumed. The grain size of the Rose Run Sandstone is in the range of fine to medium sand (Riley et al., 1993). An average grain diameter of 200 μm was assumed. The estimated reactive surface area was 1000 cm^2/g. This was calculated based on surface roughness, which is defined as the ratio of the true surface area to the equivalent geometric surface area. A surface roughness of 10 was used (White and Peterson, 1990). Interaction with the minerals is generally expected to occur only at selective sites of the mineral surface and the actual reactive surface area can be between 1 and 3 orders of magnitude less than the surface roughness-based surface area (Lasaga, 1995). The difference is attributed to the fact that only part of the mineral surface is involved in the reaction due to coating or armoring, small exposure area that is in contact with the brine, and channeling of the reactive fluid flow. A conservative reactive surface area was set at 10 cm^2/g for all mineral assemblages.

Activity coefficients were calculated using the B-dot equation (an extension of the Debye Huckle equation) (Pitzer and Brewer, 1961). The virial method (Pitzer equations) is better suited to high ionic strength solutions such as the brine under consideration (Pitzer and Brewer, 1961), but GWB's application of the Pitzer equations does not take into account the distribution of species in solution, only recognizes free ions as if each salt has fully

dissociated in solution, and doesn't take into consideration SiO_2 and Al^{3+} species. Those assumptions preclude use of GWB's Pitzer equations with minerals like albite, quartz, and feldspar. By using B-dot instead of Pitzer equations, the activity coefficients for the aqueous species are overestimated, which results in overestimates of the mass of minerals precipitated and dissolved.

3.2. Choice of variables

Reactions with three types of mineral assemblages were investigated: a carbonate assemblage composed of calcite, dolomite and siderite, which represents the carbonate layers in the aquifer; a sandstone assemblage composed of quartz, K-feldspar, kaolinite, albite, annite, and siderite, which represents the sandstone layers; and a mixed assemblage (sandstone–carbonate), which represents the aquifer as a whole. Annite was used as a proxy for glauconite due to the lack of thermodynamic and kinetic data for glauconite. The abundance of each mineral phase was compiled from Janssens (1973) and Riley et al. (1993) and recast to 10 kg of rock (Table 2).

Four brine compositions were considered. The brine composition of the Rose Run Sandstone is based on a sample from Coshocton County, Ohio (Breen et al., 1985). In addition, brine compositions from the Clinton Formation and Mt. Simon Sandstone in Ohio, and the Grand Rapids Formation in the Alberta Basin were used for comparison with the Rose Run brine (Table 3).

Brine mass was set at 0.4 kg H_2O plus total dissolved solids determined by the brine chemistry. In order to attain a porosity of 10–15% of the Rose

Table 2
The three main groups of mineral assemblages and each mineral mass recast based on a total of 10 kg rock mass

Carbonate	Weight (g)	Sandstone	Weight (g)	Mixed	Weight (g)
Dolomite	6000	Quartz	8300	Quartz	7000
Calcite	3900	K-feldspar	1000	Dolomite	1380
Siderite	100	Kaolinite	300	Calcite	800
		Albite	200	K-feldspar	500
		Annite	100	Annite	100
		Siderite	100	Albite	100
				Kaolinite	100
				Siderite	20

Table 3
Composition of Rose Run, Clinton, Grand Rapids, and Mt. Simon brines compiled from the literature

Brine species	Rose Run[a] (mg/kg)	Clinton[b] (mg/kg)	Mt. Simon[c] (mg/kg)	Grand Rapids[d] (mg/kg)
Na^+	60,122	67,000	32,000	26,539
K^+	3354	850	1060	636
Ca^{2+}	37,600	23,200	12,400	2737
Mg^{2+}	5880.6	1840	2190	533
HCO_3^-	122	200	71	182
Cl^-	191,203	160,400	78,700	47,549
SO_4^{2-}	326.4	523	1180	337
SiO_2(aq)	3	1	5.00E−07	0.00046
Al^{3+}	2.16	1	5.00E−07	0.461
Fe^{2+}	140	5	1.54	4.6E−05
Sr^{2+}	455.52	753	236	–
Br^-	3760	–	362	–
Rb^+	–	51	–	–
pH	6.4	6.5	6.65	7.2
TDS	277,571	250,000	150,000	90,000

[a] Breen et al. (1985).
[b] Lowry et al. (1988).
[c] Ohio Geological Survey (1990).
[d] Gunter et al. (2000).

Run Sandstone, the brine-to-rock ratio was set at 1:25 except in the case where the Rose Run was compared with the other three brines for which the brine-to-rock ratio was 1:10. The temperature of the system was assumed isothermal and set at 54 °C for kinetic and path of reaction simulations. In the case of the equilibrium reaction, the temperature was set at 35 °C, 54 °C and 75 °C in order to investigate the effect of temperature on the precipitation/dissolution of carbonate rocks. The model parameters and simulation conditions are given in Table 4.

The initial fugacity of CO_2 (f_{CO_2}) was set at 10 MPa for the kinetic modeling; it was varied in 2 MPa increments from 10 to 2 MPa for the equilibrium modeling, with a minimum fugacity set at 8×10^{-3} MPa. The maximum fugacity was calculated based on the maximum injection pressure that avoids rock fracturing, which is 85% of lithostatic pressure (Gunter et al., 2000). This is the maximum safe injection pressure, above which pressure-induced rock fracturing poses a risk. The lithostatic pressure in the Rose Run Sandstone ranges from 20 to 26 MPa; an injection pressure of 22 MPa was assumed for an injection depth of 1000 m. The fugacity (f_{CO_2}) varies with pressure according to the following formula:

$$f_{CO_2} = \alpha P_{CO_2} \quad (2)$$

where P_{CO_2} is the pressure of CO_2 and is equal to the injection pressure near the injection site, and α is the fugacity coefficient, which depends on pressure and temperature. The fugacity (f_{CO_2}) was calculated using the CO_2 solubility model developed by Duan and Sun (2003). The minimum fugacity of 8×10^{-3} MPa is the fugacity of dissolved HCO_3^- reported in the brine, without injection of CO_2. Initial f_{CO_2} values between 10 MPa and 8×10^{-3} MPa are intended as simple representations of the decrease in P_{CO_2} with distance from the injection site (Fig. 4). Thus, the investigation of how geochemical reactions vary as a function of initial f_{CO_2} can approximate the sequence of reactions and the reaction progress as f_{CO_2} decreases with increasing distance from the injection site and over time. Because the program considers only the CO_2 that is dissolved in the brine for a given fugacity this approach does not take into account the decrease in the saturation of the pores by free CO_2 with increasing distance from the injection site.

Table 4
Values of model parameters used in the calculations

Parameters	Description
Temperature	35 °C, 54 °C and 75 °C
CO_2	Dissolved in the brine subjected to salting-out effect
Activity coefficient (B-Dot equation)	$\log \gamma_i = -\frac{Az_i^2\sqrt{I}}{1+\dot{a}_i B\sqrt{I}} + \dot{B}I$
Reactive surface area	10 cm^2/g
Rate constants	Table 1
Porosity	12%
Brine–rock ratio	1:50, 1:25, 1:17, 1:12 and 1:10
Total rock mass	10 kg
Brine	Rose Run, Clinton, Mt. Simon and Grand Rapids
CO_2 fugacity	0.008–30 MPa

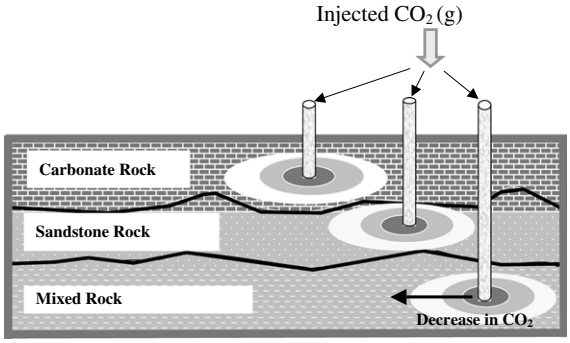

Fig. 4. Schematic diagram showing the decrease in CO_2 pressure as a function of radial distance.

Simulation begins by computing the initial equilibrium between brine and a given f_{CO_2}. The initial brine composition of the Rose Run without added CO_2 is reported in Table 3. Carbon dioxide of a given fugacity is dissolved into and equilibrated with the brine before adding mineral reactants. For example, at 10 MPa f_{CO_2}, around 0.69 molal of CO_2(aq) dissolves into original brine and the system's pH drops from 6 to 4.25. Once equilibrium is achieved between the CO_2 and the brine, reactions with mineral assemblages were simulated using equilibrium, path-of-reaction, or kinetic modeling.

4. Results

4.1. Equilibrium modeling

Fig. 5 shows the pH at equilibrium and the change in dissolved concentration of CO_2(aq) as a consequence of equilibrating the CO_2 and brine, with the minerals plotted as a function of initial f_{CO_2}. The equilibrium pH for the carbonate mineral assemblage is low (<5) for f_{CO_2} of 2 or more,

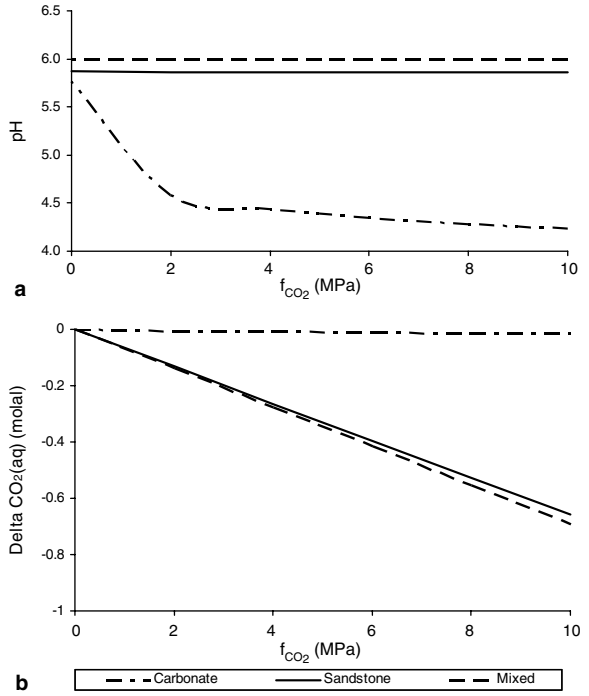

Fig. 5. Equilibrium modeling showing (a) pH as a function of f_{CO_2}, and (b) net CO_2 consumption as a function of f_{CO_2} at $T = 54$ °C.

whereas the pH in the sandstone and mixed assemblages is buffered by dissolution of silicate minerals at about 6 for all initial f_{CO_2} (Fig. 5a). Initially, the brine at equilibrium with the CO_2 contained 0.14, 0.28, 0.4, 0.58, and 0.7 molal of CO_2 for fugacities of 2, 4, 6, 8, and 10 MPa, respectively. The change in CO_2(aq) is zero over the range of fugacities studied for equilibration with the carbonate assemblage, whereas for equilibration with the silicate and mixed assemblages, for every initial f_{CO_2} all the CO_2 dissolved in the brine is consumed and trapped in the precipitated carbonate minerals (Fig. 5b).

For the sandstone and mixed assemblages, minerals dissolved and precipitated at equilibrium include both carbonate and silicate phases. For an initial f_{CO_2} of 10 MPa there is precipitation of the carbonate minerals dolomite, siderite, and strontianite and dissolution of calcite resulting in a net precipitation of 0.2 moles of carbonate minerals (Table 5). In addition, net precipitation of the silicate minerals quartz, muscovite and microcline is an order of magnitude greater than the net precipitation of carbonate minerals (Table 5). Albite, K-feldspar and kaolinite, which are not shown in the table, are completely dissolved. However, for the carbonate assemblage, there is no silicate precipitation and a net dissolution of 0.12 moles of carbonate minerals (Table 5); this net dissolution holds regardless of the initial CO_2 fugacity (Fig. 6a). In the case of the sandstone and mixed mineral assemblages, the moles of carbonate minerals precipitated at equilibrium increases from 0.01 to 0.2 as initial f_{CO_2} increases from 2 to 10 MPa (Fig. 6a). Fig. 6b shows the breakdown of the individual carbonate minerals precipitated or dissolved for the mixed assemblage. The mass of strontianite and dolomite that forms is not affected by f_{CO_2} but the mass of siderite that forms is proportional to f_{CO_2}.

The effect of temperature on the dissolution and precipitation of carbonate minerals was studied for $T = 35$, 54, and 75 °C. Temperature has little effect on reactions with the carbonate assemblage, but for the sandstone and mixed assemblages, the total mass of carbonate minerals precipitated increases with decreasing temperature (compare Figs. 6a, 7a and 8a). Figs. 6b, 7b, and 8b show the breakdown of carbonate mineral precipitation and dissolution for the mixed assemblage. The biggest difference with temperature is that more siderite forms at lower f_{CO_2} for the lower temperature simulations. Dawsonite is not a stable mineral in the equilibrium assemblages for any initial f_{CO_2} at $T = 35°$, 54° or 75 °C (Figs. 6b, 7b and 8b).

4.2. Path of reaction

Path of reaction modeling was conducted in order to understand the evolution of the system as it approaches equilibrium. Path-of-reaction modeling follows the incremental dissolution and precipitation

Table 5
Minerals precipitated or dissolved (in mole) at equilibrium for fugacity of 10 MPa

Rock assemblage	Dolomite	Calcite	Siderite	Dawsonite	Strontianite	Quartz	Muscovite/microcline
Carbonate	0.11	−0.31	0.09	0.000004	0.002	–	–
Sandstone	0.064	0	0.15	–	0.001	1.86	0.25
Mixed	0.12	−0.13	0.2	–	0.002	1.9	1.85

Minus sign indicates dissolution of mineral.

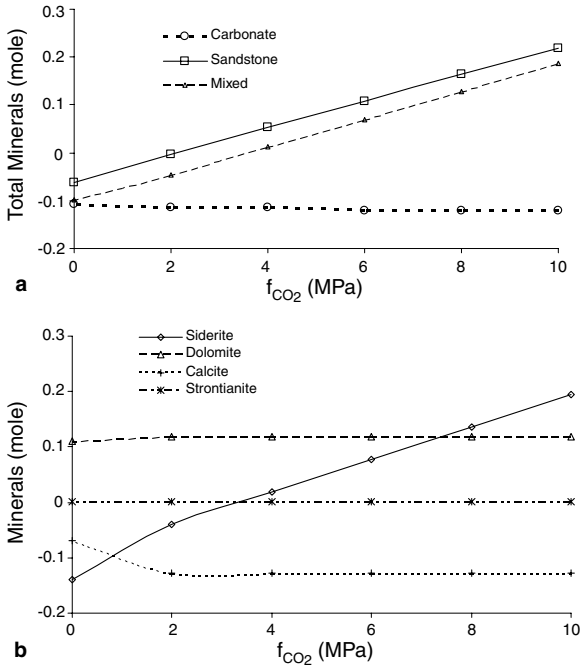

Fig. 6. Equilibrium modeling at $T = 54$ °C showing net precipitation/dissolution of carbonate minerals for (a) all three rock assemblages, and (b) mixed assemblage.

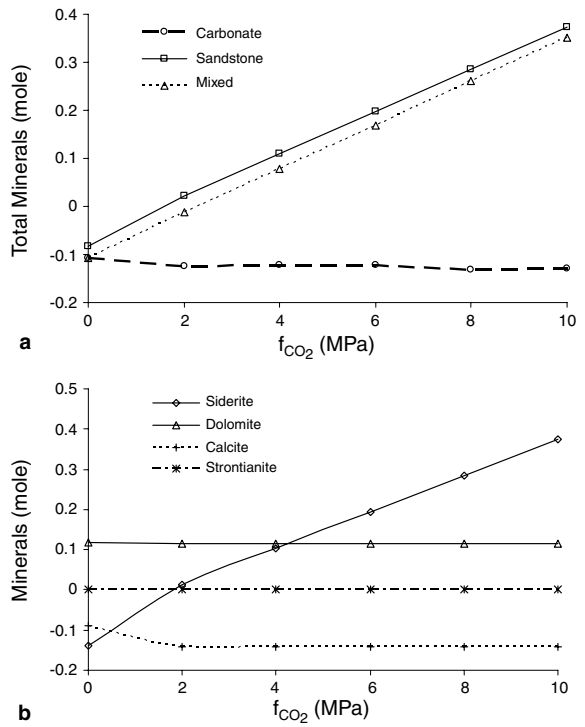

Fig. 7. Equilibrium modeling at $T = 35$ °C showing net precipitation/dissolution of carbonate minerals for (a) all three rock assemblages, and (b) mixed assemblage.

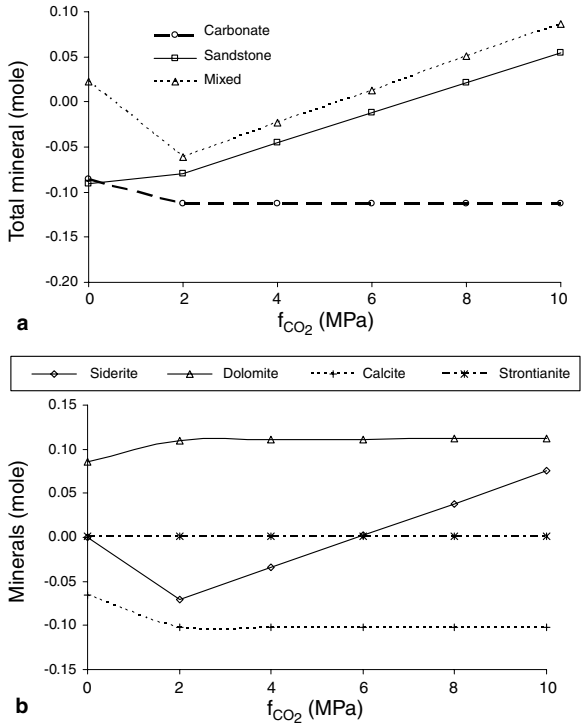

Fig. 8. Equilibrium modeling at $T = 75$ °C showing net precipitation/dissolution of carbonate minerals for (a) all three rock assemblages, and (b) mixed assemblage.

of mineral phases as the system equilibrates to small changes in composition due to the addition or removal of mineral reactants along the approach to final equilibrium. As the model reactions progress small aliquots of mineral reactant are added to the system and allowed to come to equilibrium; these steps are repeated until the total amount of reactant has been added. The measure of the reaction progress is a dimensionless number, which varies from 0 (no reactive minerals added to the system – initial state) to 1 (all reactive minerals added to the system – final equilibrium state). Fig. 9 shows the masses of dawsonite and siderite precipitated over the path of the reaction for CO_2–brine–rock reactions with the mixed assemblage and initial f_{CO_2} ranging from 2 to 30 MPa. For the initial f_{CO_2} of 2, 6, 10, and 14, dawsonite precipitated until 2.5%, 6%, 10% and 14% of mineral reactants were added to the system, respectively. When the total reactants added to the system exceeds the above percentages for the respective f_{CO_2}, dawsonite starts to dissolve such that the system at final equilibrium (100% of the reactants reacted) contains no dawsonite (Fig. 9a). For f_{CO_2} of 30 MPa, maximum quantities of dawsonite

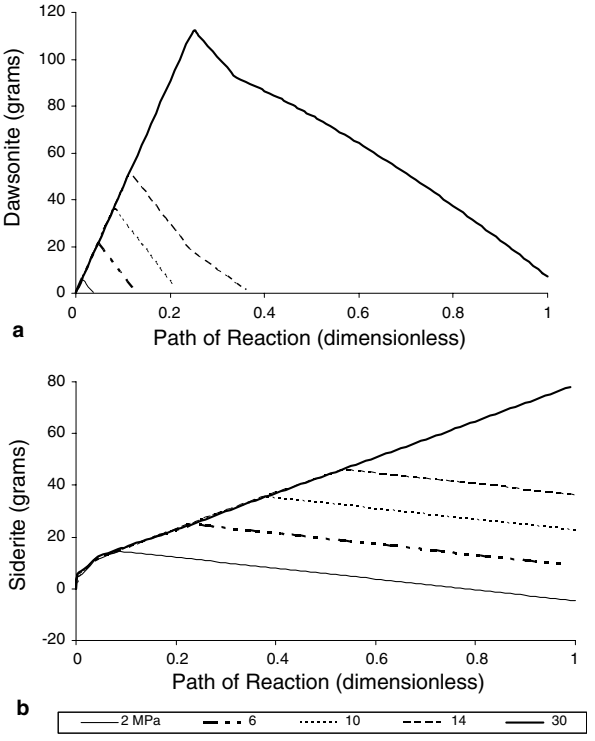

Fig. 9. Path of reaction showing the formation and dissolution of (a) dawsonite, and (b) siderite for the mixed assemblage (f_{CO_2} ranges from 2 to 30 MPa).

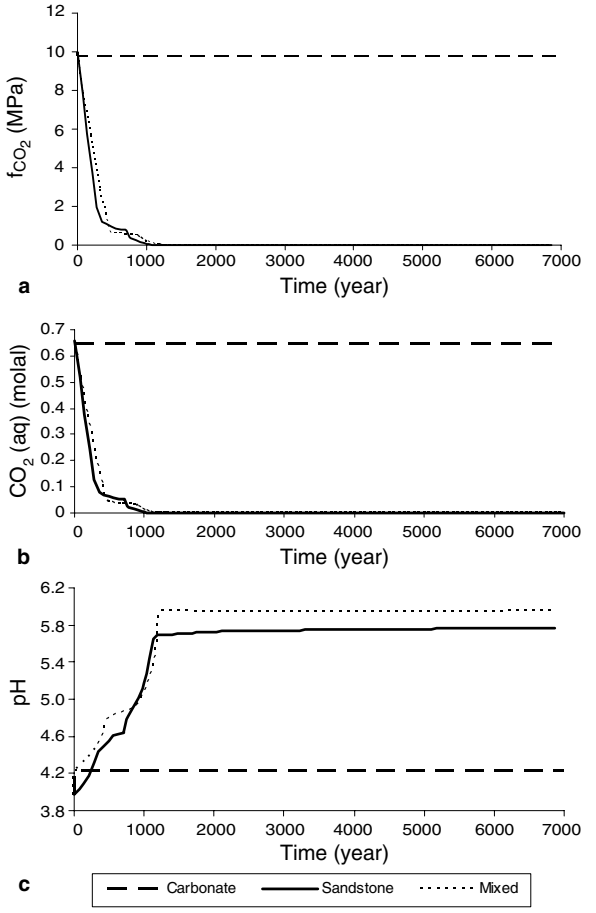

Fig. 10. Fugacity of CO_2 (a), dissolved aqueous CO_2 (b), and pH (c) as a function of time in kinetic model simulations.

precipitated correspond to 25% minerals reacted (Fig. 9a). At final equilibrium, more than three quarters of the precipitated dawsonite has dissolved.

Siderite formation shows a similar pattern over the course of reaction. The maximum amount of siderite is precipitated as the total reactants added to the system reaches 8%, 25%, 38% and 56% at initial f_{CO_2} of 2, 6, 10 and 14, respectively (Fig. 9b). As the total reactants added to the system exceeds the above percentages, siderite starts to dissolve such that at final equilibrium, the total siderite left is 110% (beside all the newly precipitated, 10% of the initial rock was also dissolved), 40%, 35% and 30% less than the maximum amount formed during the path of the reaction (Fig. 9b). For f_{CO_2} of 30 MPa, siderite is precipitated throughout the course of the reaction (Fig. 9b).

4.3. Kinetic modeling

Kinetic modeling was performed to simulate reactions over a 7 ka period. Initial f_{CO_2} was set at 10 MPa and the dispersal of CO_2 over time due to mass transfer was not considered. Fig. 10 shows the evolution of f_{CO_2} (and the corresponding aqueous CO_2 concentration) and pH through time for reactions with the carbonate, sandstone and mixed assemblages. The f_{CO_2} and the pH for the carbonate assemblage remain the same with time because there is little sequestration of CO_2 by mineral trapping and all the CO_2 in the system remains in dissolved form (Fig. 10a and b). For both the sandstone and mixed assemblages there are rapid initial declines in f_{CO_2} as a result of CO_2–brine–mineral reactions that trap the CO_2 as carbonate minerals, such that by 100 a f_{CO_2} drops by 15% and by 1 ka it drops by 99%. After 1 ka, the rate of consumption of CO_2 slows down and the pH levels off (Fig. 10a and b)

Fig. 11 shows the masses of individual minerals precipitated and dissolved over time for kinetic modeling of reactions with the carbonate, sandstone, and mixed assemblages. For the carbonate

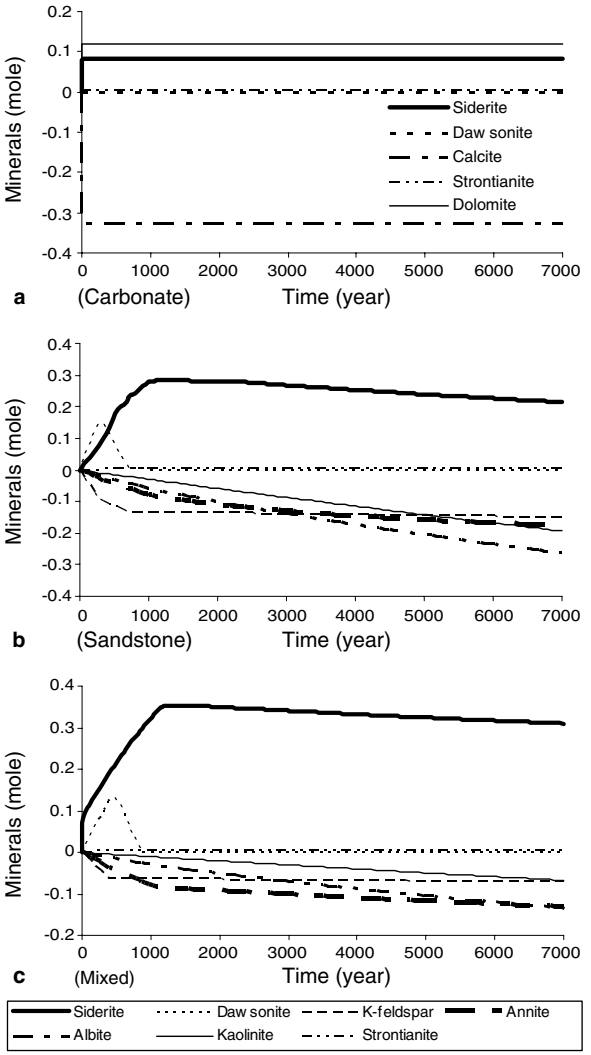

Fig. 11. Computer model results of mineral precipitation/dissolution of (a) carbonate, (b) sandstone, and (c) mixed assemblages as a function of time. (The precipitation of dolomite offsets the dissolution of calcite in both sandstone and mixed assemblage and are not included in the figure.)

rock assemblage, a small quantity of calcite dissolves rapidly over the first few tens of years and equilibrates with the brine according to the following reaction (Fig. 11a):

$$CaCO_3 + H_2O + CO_2 \leftrightarrow Ca^{2+} + 2HCO_3^- \quad (3)$$

Much of the HCO_3^- formed by the dissolution of calcite is removed from the system and trapped in the precipitated dolomite phase. In addition, a small amount of siderite, strontianite, and dawsonite quickly precipitates. However, as shown by Fig. 11a, there was no net mineral trapping of CO_2 because the precipitation of dolomite, strontianite, and dawsonite is offset by the dissolution of calcite.

For both the sandstone and the mixed rock assemblages there is precipitation of siderite, dawsonite, and strontianite, and dissolution of K-feldspar, annite, albite, and kaolinite (Fig. 11b and c). As much as 0.15 moles of dawsonite, 0.35 moles of siderite, and 0.01 moles of strontianite precipitate per 10 kg of rock reacted for both the sandstone and the mixed assemblages. The formation of dawsonite and siderite can be represented by Eqs. (4) and (5).

$$NaAlSi_3O_8 + CO_2 + H_2O \leftrightarrow NaAlCO_3(OH)_2 + 3SiO_2(aq) \quad (4)$$

$$KFe_3AlSi_3O_{10}(OH)_2 + 7CO_2 + H_2O \leftrightarrow 3FeCO_3 + 3SiO_2 + K^+ + 4HCO_3^- + Al^{3+} \quad (5)$$

In addition, dissolution of K-feldspar contributes Al, which reacts with Na in the initial brine and dissolved CO_2 to form dawsonite (Johnson et al., 2001). Dissolution of albite, K-feldspar, annite and kaolinite is driven by the decrease in pH due to dissolved CO_2. The dissolution of aluminosilicate minerals buffers the pH and provides Na, Al, and Fe needed for precipitation of carbonate minerals. Thus, precipitated masses of both siderite and dawsonite are determined by the rate of dissolution of annite, albite, K-feldspar and kaolinite. The presence of aluminosilicate phases in the sandstone and mixed assemblages significantly increases the mineral trapping potential relative to the carbonate assemblage, provided there is sufficient time for the reactions to occur.

The amount of CO_2 trapped in carbonate minerals over time is also controlled by the brine-to-rock ratio of the system (Figs. 12 and 13). The pH decreases and the f_{CO_2} increases as the brine-to-rock ratio increases (Fig. 12). The pH for a brine-to-rock ratio of 1:50 rises from 4 to 6 and then stabilizes by about 500 a, whereas the pH for the brine-to-rock ratio 1:10 rises from 4 to 4.7 and then continues to rise slowly throughout the 7 ka duration of the simulation (Fig. 12a). The higher brine–rock ratios sequester more CO_2 in the carbonate minerals dawsonite and siderite (Fig. 13a and b); the difference is particularly striking for dawsonite. The modeling shows that dawsonite is stable at lower pH values than siderite. Once aluminosilicate dissolution drives the pH sufficiently high, dawsonite begins to dissolve. The impact of reactions on pH is more

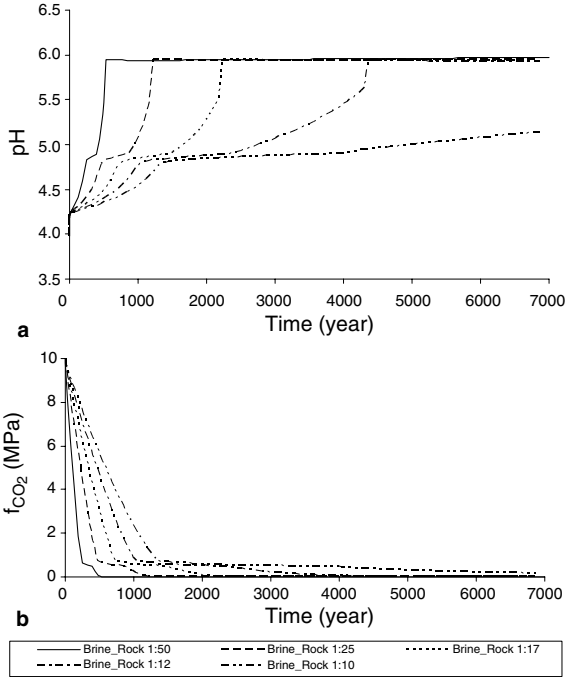

Fig. 12. Kinetic modeling for a range of brine-to-rock ratio (a) pH and (b) f_{CO_2}.

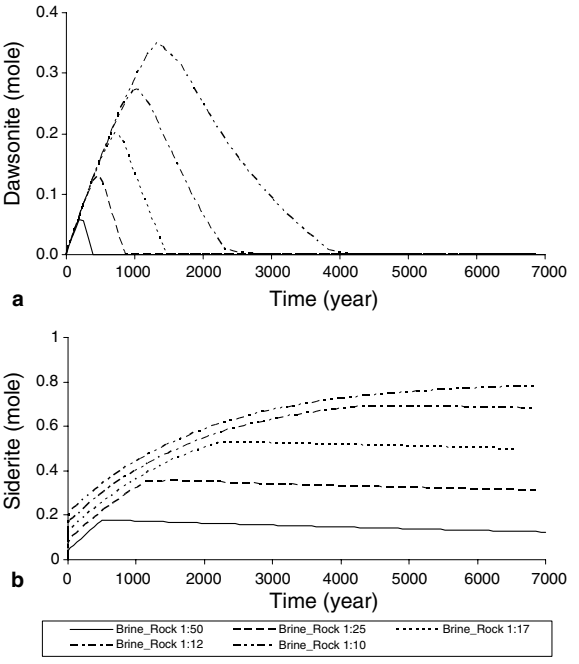

Fig. 13. Kinetic modeling for a range of brine-to-rock ratio that shows precipitation of (a) dawsonite and (b) siderite.

pronounced and more rapid for lower brine-to-rock ratios than for higher brine-to-rock ratios because there is less total CO_2 available.

Model results for four different brine compositions and a brine–rock ratio of 1:10 are shown in Fig. 14 for the mixed rock assemblage. The fugacity of CO_2 decreases rapidly for the first 500 a for the Rose Run brine, 1.8 ka for the Clinton brine and 2.2 ka for both the Mt. Simon and Grand Rapids brines. More CO_2 gas was consumed in both the Grand Rapids and Mt. Simon brines compared to the Rose Run and Clinton brines (Fig. 14a) because more dawsonite was formed from reactions with the former brines than the latter (Fig. 14b). The important factor that plays a role is the degree of salinity of the four different brine compositions. Both Grand Rapids and Mt. Simon brines are less saline (7% and 11% by weight, respectively) than the Rose Run and Clinton brines (23% and 18% by weight, respectively) (Table 3). More CO_2 dissolves in the less saline brines. For the Rose Run, Clinton, Mt.

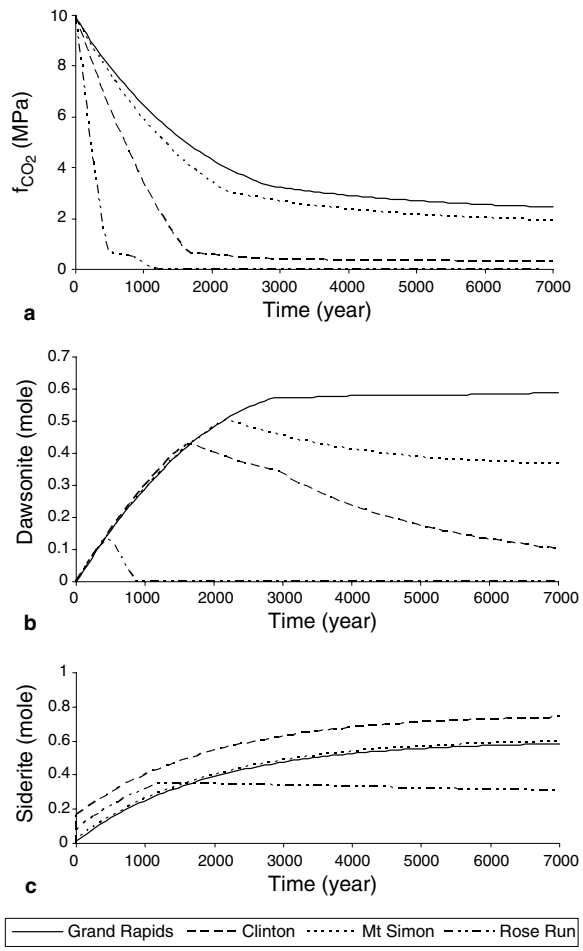

Fig. 14. Different brine composition for mixed rock assemblage (a) uptake of CO_2, (b) precipitation of dawsonite, and (c) precipitation of siderite.

Simon and Grand Rapids brines, the dawsonite abundance peaks at 0.5, 1.8, 2.2 and 3.0 ka, respectively, and then it starts to dissolve (Fig. 14b). This pattern is also captured by siderite precipitation and dissolution in the Rose Run brine (Fig. 14c). Dawsonite is stable at lower pH than siderite (Fig. 20). The pH of the Rose Run brine stabilized quickly at 6 and forced dawsonite to dissolve. The pH of all the other brines remains within 4.5–5.2. The siderite continues to precipitate as long as it is within the siderite's pH stability field. The disequilibrium of the initial Clinton brine with the host rock results in a large amount of siderite precipitation as shown at time zero in Fig. 14c.

5. Impact of reaction rates

The impact of rate constants on the overall CO_2 consumption through carbonate mineral precipitation was evaluated using the mixed mineral assemblage and rate constants that were increased and decreased by a factor of 100 compared to those listed in Table 1 (Figs. 18 and 19). Because all the rate constants were changed by the same magnitude, the effect is to compress or extend the time over which

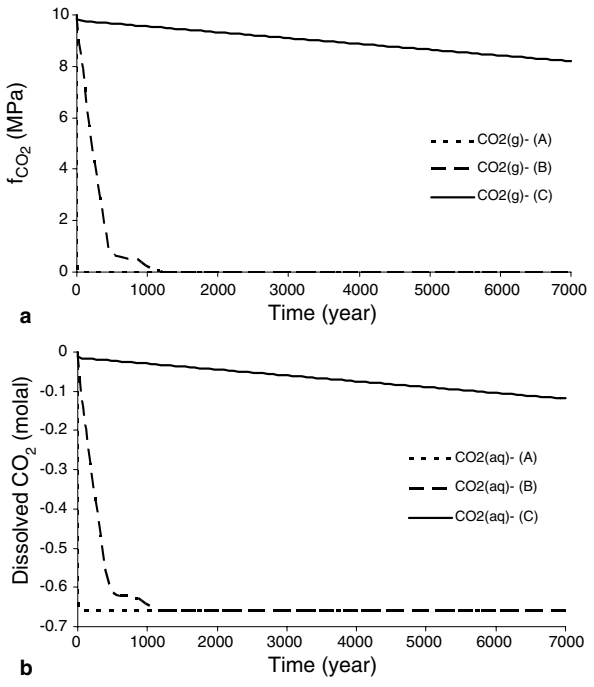

Fig. 15. Kinetic modeling of mixed rock assemblage showing (a) fugacity, and (b) dissolved CO_2 as a function of time. CO_2(g, aq) – (A), (B) and (C) are based on rate constants two magnitudes higher than Table 1, Table 1, and two magnitudes less than Table 1, respectively.

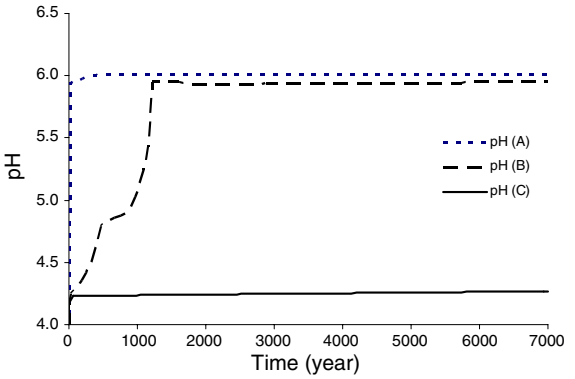

Fig. 16. Kinetic modeling of mixed rock assemblage showing pH as a function of time. The pH (A), (B) and (C) are based on rate constants two magnitudes higher than Table 1, Table 1, and two magnitudes less than Table 1, respectively.

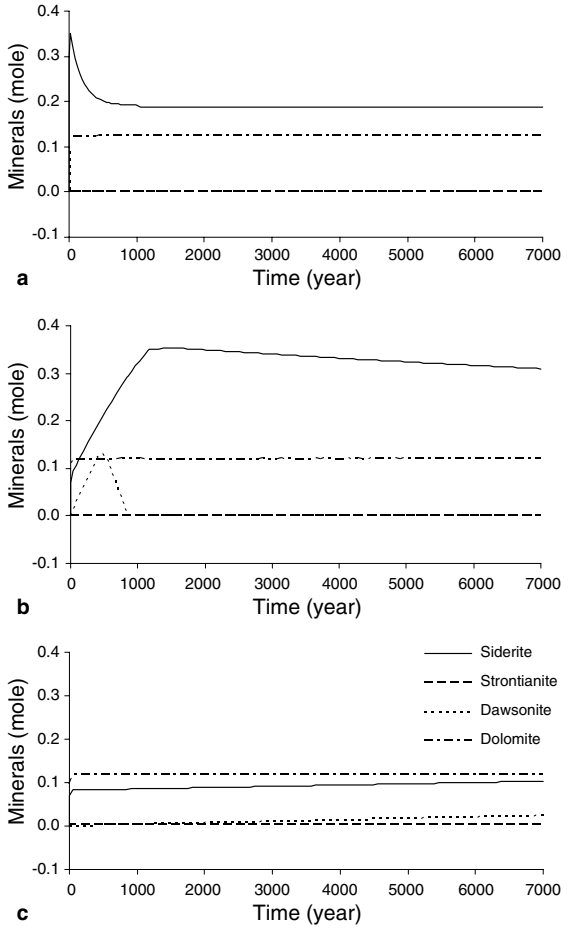

Fig. 17. Kinetic modeling of mixed rock assemblage showing carbonate minerals precipitated based on rate constants (a) two magnitudes higher than Table 1, (b) Table 1, and (c) two magnitudes less than Table 1.

minerals dissolve and precipitate, but not to alter the relative timing of mineral precipitation and dissolution. Application of lower rate constants forced the system to be dominated by aqueous CO_2 with only 15% of the added CO_2 consumed after 7 ka (Fig. 15a and b). Increasing the rate constants by a factor of 100 caused all the added CO_2 to be consumed within 10 a (Fig. 15a and b) in contrast to 1 ka for the rate constants listed in Table 1. The temporal evolution of pH (Fig. 16) reflects the amount of CO_2 that remains dissolved in the system. With lowered rate constants and slower uptake of CO_2 by carbonate precipitation, the pH of the brine remains less than 4.3 for the 7 ka duration of the simulation. Using increased rate constants, the pH of the brine rises above 6.0 within 10 a (Fig. 16).

Minerals subject to net precipitation at the end of the simulation are shown in Fig. 17. For rate constants assigned in Table 1, siderite and dawsonite precipitate for hundreds of years (0.5 ka for dawsonite and 1 ka for siderite) and then begin to dissolve. The dawsonite dissolves completely, but 0.3 moles of siderite remain at the end of the simulation (Fig. 17b). With rate constants increased by a factor of 100, dawsonite precipitates and completely dissolves within a few years. For increased rate constants, the timescale over which siderite precipitates is reduced to a few years (Fig. 17a), but following a period of dissolution, siderite abundance stabilizes at 0.2 moles after 1 ka (Fig. 17a). Siderite and dawsonite precipitate for the entire 7 ka duration of the simulation when the rate constants are decreased by a factor of 100 (Fig. 17c).

Minerals subject to net dissolution at the end of the simulations are shown in Fig. 18. Over the duration of the simulation, dissolution of K-feldspar, albite and kaolinite is strongly impacted by changing rate constants (compare Fig. 18a–c). Calcite dissolves rapidly during the first few years then stabilizes at 0.33 moles dissolved for the rest of the simulation for modeling based on rate constants in Table 1 and for decreased rate constants (Fig. 18b

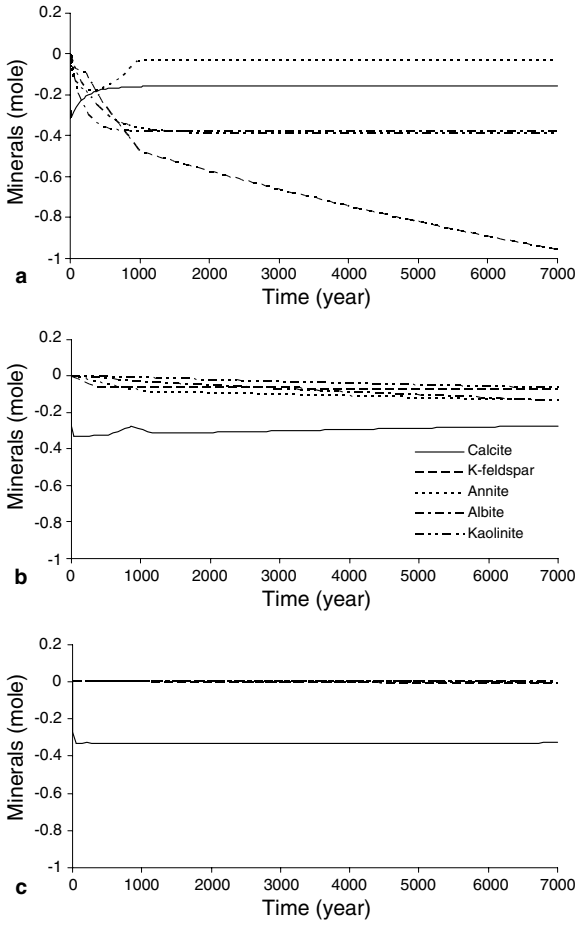

Fig. 18. Kinetic modeling of mixed rock assemblage showing minerals dissolved based on rate constants (a) two magnitudes higher than Table 1, (b) Table 1, and (c) two magnitudes less than Table 1.

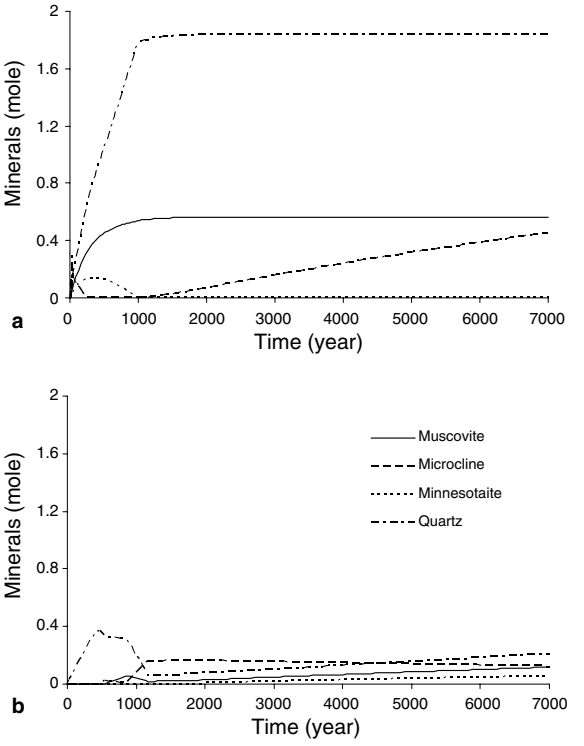

Fig. 19. Kinetic modeling of mixed rock assemblage showing silicate minerals precipitated based on rate constants (a) two magnitudes higher than Table 1, and (b) Table 1.

and c). The simulation using the increased rate constants shows initial rapid calcite dissolution followed by re-precipitation of calcite as silicate dissolution brings the pH into the calcite stability field. Calcite abundance stabilizes at a net of 1.6 moles dissolved after 1 ka. Annite also dissolves for the first 400 a and then re-precipitates until it stabilizes at a net of 0.03 moles dissolved after 1 ka (Fig. 18a). Excess Fe derived from the dissolution of annite (Fig. 18a) does not contribute to siderite precipitation, but instead is trapped in the mica group mineral: Minnesotaite (Fig. 19a).

Silicates minerals precipitated throughout the simulation period are shown in Fig. 19. The increase in rate constants precipitates a large amount of quartz within the first 1 ka before quartz abundance peaks at 1.8 moles (Fig. 19a). At the end of 7 ka, the precipitation of quartz, muscovite, and microcline increase by a factor of 2–4.5 (Fig. 19a and b). A large amount of minnesotaite is precipitated within the first 1 ka when the rate constants increase by a factor of 100. When the pH increases, minnesotaite is completely dissolved after the 1 ka mark.

6. Discussion

Equilibrium, path of reaction, and kinetic modeling simulates geochemical reactions and the fate of CO_2 thousands of years after injection. The pH at equilibrium for reactions with the carbonate assemblage decreases with increasing initial f_{CO_2} because more CO_2 is dissolved in the brine and the pH is not completely neutralized by reactions with carbonate minerals. This relationship suggests that adding CO_2 into a carbonate formation will increase acidity and dissolve, not precipitate, carbonate minerals. The CO_2 remains as dissolved aqueous species such that the carbonate layers of the Rose Run are unlikely to contribute to mineral trapping of CO_2. The dominant CO_2 sequestration mechanisms in carbonate host rocks are solubility and hydrodynamic trapping.

In contrast, for both the sandstone and mixed assemblages the amount of CO_2 trapped in carbonate minerals at equilibrium increases as the f_{CO_2} increases (Figs. 6a, 7a, and 8a). The most important minerals for trapping CO_2 in the Rose Run Sandstone are dawsonite ($NaAlCO_3(OH)_2$) and siderite ($FeCO_3$). Precipitation of these carbonate minerals requires that sufficient amounts of Na, Fe and Al be available for reaction. These ions are added to brine by dissolution of aluminosilicate minerals in response to the increase in acidity with the addition of CO_2. In addition, the Na needed for dawsonite precipitation is available in great quantities in the initial brine. Albite dissolution contributes additional Na and Al, and K-feldspar dissolution contributes Al to the brine. Dissolution of the mineral glauconite, which is inhomogeneously distributed, but locally very abundant in the Rose Run Sandstone, contributes Fe. That contribution was simulated here by dissolution of the mineral annite. In addition to providing sources of Na, Fe and Al, dissolution of aluminosilicate minerals neutralizes the acid formed by dissolution of CO_2 into the brine. Dissolution of CO_2 and carbonate precipitation (magnesite and siderite) was confirmed experimentally at 200 °C and 20 MPa by Kaszuba et al. (2003, 2005).

Dawsonite and siderite are likely to be very important for mineral trapping of CO_2 in many deep saline aquifers, like the Rose Run Sandstone, which are otherwise suitable for geologic sequestration but lack abundant sources of Ca, Mg and Sr that are necessary to induce precipitation of the carbonate minerals calcite, dolomite, and strontianite. Consequently, understanding the controls on dawsonite and siderite formation is very important. The equilibrium, path-of-reaction, and kinetic modeling demonstrate that the mass of these minerals precipitated depends strongly on initial f_{CO_2}, temperature, the brine-to-rock ratio, and the kinetic rate of silicate mineral dissolution and time for reaction.

Specifically, equilibrium modeling shows that dawsonite does not precipitate in the final equilibrium assemblage for simulations conducted across the range of initial f_{CO_2} and the range of model temperatures. The path of reaction modeling, however, demonstrates that for all initial f_{CO_2} studied, dawsonite precipitates during the initial stages of the reactions, when little mineral has reacted with the system, but dissolves as the reaction proceeds to completion (Fig. 9). This pattern of initial precipitation of dawsonite followed by dissolution is repeated by the kinetic modeling. For an initial f_{CO_2} of 10 MPa, dawsonite precipitates for the first ≈300 a for the sandstone assemblage and more slowly for the mixed assemblage for ≈600 a, after which time it begins to dissolve (Fig. 11b and c). The time period over which precipitation takes place and the total amount of dawsonite precipitated increase as brine-to-rock ratio increases (Fig. 13a).

Initial f_{CO_2} controls how much CO_2 is available in the model system for reaction and consequently the evolution of the pH over the course of the reaction. The transition from dawsonite precipitation to dawsonite dissolution with progress along the path of reaction reflects the consumption of the acidic CO_2 by CO_2–brine–mineral reactions, and the resulting elevation of pH. The higher the initial f_{CO_2} the more reaction is necessary to consume the CO_2 dissolved in the brine to the point where dawsonite is unstable. Increasing brine-to-rock ratio has the same effect as increasing f_{CO_2} by increasing the amount of CO_2 available relative to the amount of minerals to react with it. Thus, the equilibrium, path-of-reaction, and kinetic modeling show that dawsonite is thermodynamically less stable at lower f_{CO_2} and corresponding higher pH values. Patterns of siderite formation and dissolution are similar to those for dawsonite, but siderite is more stable than dawsonite at lower f_{CO_2} and higher pH, and at higher temperatures.

The effect of pH as a function of both $NaHCO_3$ and HCO_3^- on the stability of dawsonite and siderite are given in Fig. 20. The activities of $NaHCO_3$ and HCO_3^- range between 1 and 10^{-5}. The activity of Fe^{2+} is 0.005–0.2, whereas that of Al^{3+} is 10^{-6}–10^{-12}. The stability field of dawsonite (Fig. 20a) corresponds with the observed trend of precipitation and dissolution of dawsonite. The higher the activity of the HCO_3^- the lower the pH is, and dawsonite is stabilized (Fig. 19a). However, increasing the pH, which is decreasing the activity of HCO_3^- forces dawsonite to dissolve as shown in the equilibrium, path of reaction and kinetic modeling. Siderite also shows the same pattern: the higher the HCO_3^- the lower the pH and it is stabilized in a larger field of pH as compared to dawsonite (Fig. 20b). At higher pH (Figs. 10c and 11b and c), siderite starts to dissolve in agreement with the stability field shown in Fig. 20b.

Because laboratory measurements of rate constants may differ by several magnitudes from the actual field reaction rates, rate of reaction is another important unknown that could greatly impact masses and forms of mineral trapping of CO_2. As shown in Figs. 18 and 19, the modeling is very sensitive to the rate constant and an increase or decrease of two orders of magnitudes can produce a large difference in the consumption CO_2 through carbonate minerals. The CO_2 trapped in carbonate minerals falls by a factor of 2–3 if the rate constants decrease by two orders of magnitudes (compare

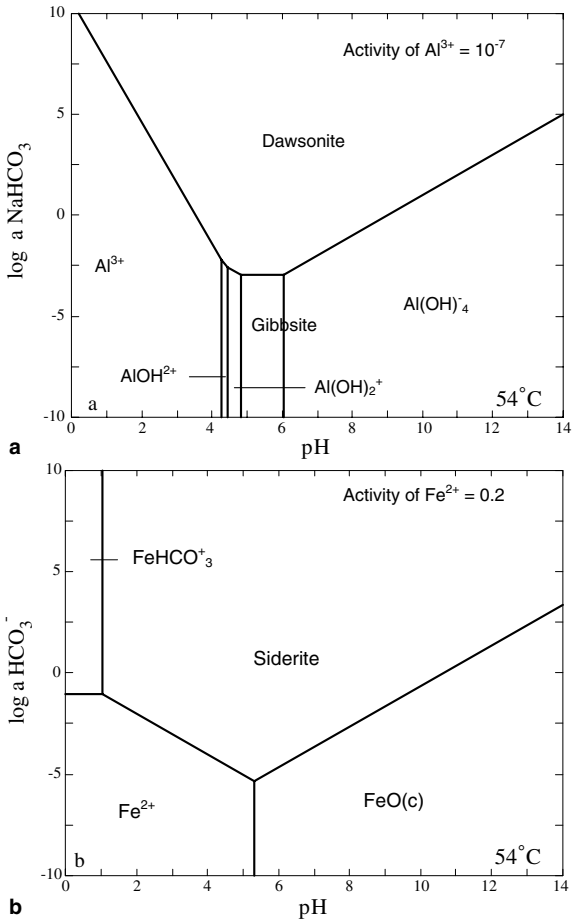

Fig. 20. Stability field of (a) dawsonite and (b) siderite as a function of pH and both $NaHCO_3$ and HCO_3^-.

Fig. 17b, and c). On the other hand, increasing the rate constants by a magnitude of two enhances the CO_2 trapping mechanism through carbonate mineral precipitation within the first 1 ka (Fig. 17a and b). For the time scale above 1 ka, the added CO_2 was completely consumed in the modeling scenarios (Figs. 15a, b, 16 and 17a and b). The large uptake of CO_2 through siderite precipitation in Fig. 17b is compensated by the small amount of calcite dissolution in Fig. 18a.

High f_{CO_2} is expected in close proximity to the injection site and immediately following injection. Carbon dioxide fugacity decreases with distance from the injection site and over hundreds of years after injection due to dispersion and migration. Given dawsonite's increasing stability at higher f_{CO_2} and the kinetic modeling results that indicate relatively rapid precipitation of dawsonite during the first 1 ka, dawsonite is predicted to be particularly

important in converting mobile, dissolved CO_2 into immobile minerals in the Rose Run Sandstone. Over time, as f_{CO_2} decreases, dawsonite may begin to dissolve as predicted by thermodynamic simulations. However, kinetic inhibitions may slow or prevent the dissolution. For example, dawsonite remains present in great abundance in the Sydney Basin of Australia today, millions of years after the magmatic CO_2 that induced its precipitation dissipated (Baker et al., 1995). Even as the dawsonite dissolves, however, siderite remains stable and continues to precipitate, taking up some of the re-released CO_2.

Near the injection well, most of the pores are filled with CO_2 as water is displaced during the injection. Some water will be trapped within the pore that can facilitate reaction between CO_2 and the host rock. The modeling suggests that if calcite is present as cement near the injection site, it is more likely to dissolve in small quantities (Fig. 10a). When CO_2 gas comes in contact with water, it dissolves in water to from H_2CO_3. Due to its acidity, it will dissociate into H^+ and HCO_3^- and the free H^+ ion will cause calcite to dissolve. However, the dissolution of calcite is accompanied by the precipitation of silicate minerals, like quartz and microcline (Fig. 19b). This will greatly affect the porosity and permeability of the formation. The dissolution of carbonate mineral may be offset by the precipitation of silicate minerals resulting in a net small decrease in porosity. However, the effect on permeability depends greatly on where the dissolution and/or precipitation occur within the pore space.

The modeling conducted here does not take into account free CO_2, which will displace brine as it is injected. This displacement decreases the amount of brine in the pore space and therefore the brine-to-rock ratio with approach to the injection site. Although the modeling indicates a decrease in the mass of carbonate minerals precipitated with decreasing brine-to-rock ratio, it is expected that this effect will have little impact once free CO_2 is included in the system. Free CO_2 in the pore space provides a large source of additional CO_2 that was not considered in the model approach. The equilibrium modeling indicates that for f_{CO_2} of 10 MPa and $T = 54\,^{\circ}C$, all the CO_2 dissolved in the brine is consumed by reactions with formation minerals (Fig. 5b). With more free CO_2 available to dissolve into the brine, more aluminosilicate minerals would react with the aqueous CO_2 and carbonate mineral precipitation would be increased. In terms of the path of reaction and kinetic modeling, the impact of including free CO_2 would be to increase the percentage of the reaction or the time period over which dawsonite precipitation is favored.

Significant amounts of carbonate rock (10–40 g) were precipitated. Large amount of initial silicate minerals dissolved and secondary silicate minerals precipitated. Overall, the equilibrium and kinetic modeling predicts a net rock mass gain of 10–20 g at f_{CO_2} of 10 MPa, for the sandstone assemblage. The gain in mass is accompanied by an uptake of 1.5–2 g of CO_2 per kg of reacted rock. The majority of the net gain in rock mass is due the precipitation of quartz, muscovite, and microcline in response to release of silica from dissolving K-feldspar, kaolinite and albite. The increase in rock mass is accompanied by a decrease in porosity of 0.1–0.2%, which has the potential both to cause clogging, slowing injection, or, on the positive side, can improve the cap rock sealing. Thus, constraints on the rates and products of the CO_2–brine–mineral reactions are very important for understanding the long time effect on the safety and integrity of the seal of the formation.

7. Conclusions

Evaluating the long-term geochemical behavior of the injected CO_2 and its possible impact on the integrity of the formation is a crucial aspect of geological CO_2 sequestration safety assessment. Computer simulations using the computer program 'Geochemist's Workbench' were used to model the equilibrium and kinetic assemblages produced by reacting typical Rose Run carbonate, sandstone, and mixed mineral assemblages with measured brine compositions. Although the computer code has no transport component to it, the effects of radially decreasing CO_2 pressure from an injection site were investigated in a simplistic way by varying CO_2 fugacity. This modeling of the chemical reactions under no-flow conditions provides insight into what parameters control the reactions and their final products. The results of equilibrium model demonstrate that dissolution of albite, K-feldspar, and glauconite and the precipitation of siderite and dawsonite are potentially very important for mineral trapping of CO_2. The mass of dawsonite and siderite precipitated depends on mineral assemblage composition, brine composition, temperature, and initial CO_2 fugacity; initial

CO_2 fugacity and brine composition have by far the greatest impact. Dawsonite and siderite are more stable at lower pH conditions. As the reactions progress and the CO_2 added to the brine are consumed, dawsonite begins to dissolve and precipitation of siderite levels off. Consequently, in order to predict the quantity of CO_2 sequestered by mineral trapping it is crucial to know the rates of the geochemical reactions relative to the rate of migration of CO_2 away from the injection site, which will determine how much CO_2 is available for reaction. Similarly, the kinetic modeling indicates that over hundreds to thousands of years it should be possible to sequester large quantities of CO_2 by mineral trapping in the sandstone and mixed units of the Rose Run Sandstone, but over tens to hundreds years solubility trapping plays the most crucial role. The time scale of the chemical reaction is very sensitive to the rate constants.

This work demonstrates that the Rose Run Sandstone has a suitable mineral composition for significant mineral trapping of CO_2. However, it also indicates that the extent of mineral trapping will be sensitive to the initial injected f_{CO_2}, the brine-to-rock ratio, the initial brine composition, and the rate of reaction. The brine-to-rock ratio, the kinetic rate of reaction, and the f_{CO_2} has a strong impact on the pH and saturation index of the precipitated/dissolved minerals. Quartz, muscovite and microcline minerals are by far the dominant phases precipitated because of the reactions and, if the reactions are fast enough; these minerals have the potential to cause clogging, slowing injection, or can locally improve the cap rock sealing capacity. As the equilibrium, path of reaction, and kinetic modeling indicate, high CO_2 fugacity is needed for mineral trapping and consequently reactions must be fast enough to reach carbonate phase saturation before the CO_2 is overly diluted by outward radial flow and diffusion.

Acknowledgment

Research on the carbon storage potential of the Rose Run Sandstone is supported by grants from the Ohio Coal Research Consortium.

References

Acker, J.G., Bricker, O.P., 1992. The influence of pH on biotite dissolution and alteration kinetics at low temperature. Geochim. Cosmochim. Acta 56, 3073–3092.

Bachu, S., 2002. Sequestration of CO_2 in geological media in response to climate change: road map for site selection using the transform of the geological space into CO_2 phase space. Energy Convers. Manage. 43, 87–102.

Bachu, S., Gunter, W.D., Perkins, E.H., 1994. Aquifer disposal of CO_2: hydrodynamic and mineral trapping. Energy Convers. Manage. 35, 269–279.

Baker, J.C., Bai, G.P., Golding, S.D., Hamilton, P.J., Keene, J., 1995. Continental-scale magmatic carbon-dioxide seepage recorded by dawsonite in the Bowen–Gunnedah–Sydney Basin system, eastern Australia. J. Sed. Res. 65, 522–530.

Bergman, P.D., Winter, E.M., 1995. Disposal of CO_2 in aquifers in the US. Energy Convers. Manage. 36, 523–526.

Bergman, P.D., Winter, E.M., Chen, Z.Y., 1997. Disposal of power plant CO_2 in depleted oil and gas reservoirs in Texas. Energy Convers. Manage. 38, S211–S216.

Bethke, C.M., 1996. Geochemical Reaction Modeling. University Press, New York.

Breen, K.J., Angelo, C.G., Masters, R.W., Sedam, A.C., 1985. Chemical and isotopic characteristics of brines from three oil- and gas-producing formations in eastern Ohio, with applications to the geochemical tracing of brine sources: USGS Water-Resources Investigations Report 84-4314.

Busenberg, E., Plummer, L.N., 1982. The kinetics of dissolution of dolomite in CO_2–H_2O systems at 1.5–65 °C and 0–1.0 atm P_{CO_2}. Am. J. Sci. 282, 45–78.

Drange, H., Alendal, G., Johannessen, O.M., 2001. Ocean release of fossil fuel CO_2: a case study. Geophys. Res. Lett. 28, 2637–2640.

Duan, Z., Sun, R., 2003. An improved model calculating CO_2 solubility in pure water and aqueous NaCl solutions from 273 to 533 K and from 0 to 2000 bar. Chem. Geol. 193, 257–271.

Gunter, W.D., Wiwchar, B., Perkins, E.H., 1997. Aquifer disposal of CO_2-rich greenhouse gases: extension of the time scale of experiment for CO_2-sequestering reactions by geochemical modeling. Mineral. Petrol. 59, 121–140.

Gunter, W.D., Perkins, E.H., Hutcheon, I., 2000. Aquifer disposal of acid gases: modeling of water-rock reactions for trapping of acid wastes. Appl. Geochem. 15, 1085–1095.

Gupta, N., Bair, E.S., 1997. Variable-density flow in the midcontinent basin and arches region of the United States. Water Resour. Res. 33, 1785–1802.

Gupta, N., Jagucki, P., Sminchak, J., Meggyesy, D., Janosy, R., Dooley, J., Bradbury, J., Spane, F., 2004. The Ohio River valley CO_2 storage project-characterization of site-specific sequestration potential. In: Proc. 3rd Ann. Conf. Carbon Capture and Sequestration, Alexandria, VA, 3–6 May 2004.

Helgeson, H.C., 1969. Thermodynamics model of hydrothermal systems at elevated temperatures and pressures. Am. J. Sci. 267, 729–804.

Helgeson, H.C., Murphy, W.M., Aagaard, P., 1984. Thermodynamics and kinetic constraints on reaction rates among mineral and aqueous solutions. II. Rate constants, effective surface area, and the hydrolysis of feldspar. Geochim. Cosmochim. Acta 48, 2405–2432.

Holloway, S., 2001. Storage of fossil fuel-derived carbon dioxide beneath the surface of the Earth. Ann. Rev. Energy Environ. 26, 145–166.

Janssens, A., 1973, Stratigraphy of the Cambrian and lower Ordovician rocks of Ohio, Ohio Department of Natural Resources, Division of the Geological Survey, Bull., 64.

Johnson, J.W., Nitao, J.J., Steefel, C.I., Knauss, K.G., 2001. Reactive transport modeling of geologic CO_2 sequestration in saline aquifers: the influence of intra-aquifer shales and the relative effectiveness of structural, solubility, and mineral trapping during prograde and retrograde sequestration. In: Proc. 1st National Conf. Carbon Sequestration, Washington, DC, 14–17 May 2001.

Kaszuba, P.J., Janecky, R.D., Snow, G.M., 2003. Carbon dioxide reaction processes in a model brine aquifer at 200 °C and 200 bars: implications for geologic sequestration of carbon. Appl. Geochem. 18, 1065–1080.

Kaszuba, P.J., Janecky, R.D., Snow, G.M., 2005. Experimental evaluation of mixed fluid reactions between supercritical carbon dioxide and NaCl brine: relevance to the integrity of a geologic carbon repository. Chem. Geol. 217, 277–293.

Klusman, R.W., 2003. Evaluation of leakage potential from a carbon dioxide EOR/sequestration project. Energy Convers. Manage. 44, 1921–1940.

Lackner, K.S., 2002. Carbonate chemistry for sequestering fossil carbon. Ann. Rev. Energy Environ. 27, 193–232.

Lasaga, A.C., 1995. Fundamental approaches in describing mineral dissolution and precipitation rates. In: White, A.F., Brantley, S.L. (Eds.), Chemical Weathering Rates of Silicates Minerals, Reviews in Mineralogy, vol. 31. BookCrafters, Chelsea, MI, pp. 23–86.

Lowry, R.M., Faure, G., Mullet, D.I., Jones, L.M., 1988. Interpretation of chemical and isotopic compositions of brines based on mixing and dilution, "Clinton" Sandstones, Eastern Ohio, USA. Appl. Geochem. 3, 177–184.

Ohio Geological Survey, 1990. Water chemistry of Mount Simon.

Pitzer, K.S., Brewer, L., 1961. In: Lewis, G.N., Randall, M. (Eds.), Revised Edition of Thermodynamics, second ed. MacGraw-Hill, New York.

Plummer, L.N., Parkhurst, D.L., Wigley, T.M.L., 1978. The kinetics of calcite dissolution in CO_2–water systems at 5–60 °C and 0.0–1.0 atm CO_2. Am. J. Sci. 278, 176–216.

Riley, R.A., Harper, J.A., Baranoski, M.T., Laughrey, C.D., Carlton, R.W., 1993. Measuring and predicting reservoir heterogeneity in complex deposystems: the late Cambrian Rose Run Sandstone of Eastern Ohio and Western Pennsylvania. US Department of Energy.

Rimstidt, J.D., Barnes, H.L., 1980. The kinetics of silica–water reactions. Geochim. Cosmochim. Acta 44, 1683–1699.

Seneviratne, G., 2003. Global warming and terrestrial carbon sequestration. J. Biosci. 28, 653–655.

Sverdrup, H.U., 1990. The kinetics of base cation release due to chemical weathering. Lund University Press, Lund.

White, A.F., Peterson, M.L., 1990. Role of reactive surface area characterization in geochemical models. Chemical modeling of aqueous systems II. In: Melchior, D.C., Bassett, R.L. (Eds.). Am. Chem. Soc. Symp. Ser. 416, 416–475.